

Improved thermochromic properties in bilayer films of VO₂ with ZnO, SnO₂ and WO₃ coatings for energy efficient glazing.

Işıl Top,^{a,b*} Russell Binions,^{a,b§} Christian Sol,^c Ioannis Papakonstantinou,^c Marcin Holdynski,^d Sofia Gaiaschi^e and Isaac Abrahams^{b,f*}

^a School of Engineering and Materials Science, Queen Mary University of London, Mile End Road, London E1 4NS, United Kingdom

^b Materials Research Institute, Queen Mary University of London, Mile End Road, London E1 4NS, United Kingdom

^c Department of Electronic and Electrical Engineering, University College London, Torrington Place, London WC1E 7JE, United Kingdom

^d Institute of Physical Chemistry, Polish Academy of Sciences, ul. Kasprzaka 44/52, 01-224 Warsaw, Poland

^e Horiba Scientific, Horiba France SAS, Avenue de la Vauve, Passage Jobin Yvon, CS 45002 – 91120 Palaiseau, France

^f School of Biological and Chemical Sciences, Queen Mary University of London, Mile End Road, London E1 4NS, United Kingdom

* Authors to whom correspondence should be addressed

Email: i.top@qmul.ac.uk; Tel: +44 (0) 20 7882 5305

Email: i.abrahams@qmul.ac.uk; Tel +44 (0) 20 7882 3235

§Deceased

Keywords: Thermochromic, vanadium dioxide, thin film, AACVD, sol-gel, zinc oxide, tin dioxide, tungsten trioxide, energy efficient windows, bilayer, antireflection.

Abstract

The thermochromic properties of bilayer films consisting of a nanostructured VO₂ under-layer and top-layers of ZnO, SnO₂ or WO₃ are presented. In each case, the VO₂ under-layer was deposited by electric field assisted AACVD on a fluorine doped tin oxide coated glass substrate, with the metal oxide top-layer deposited using sol-gel spin coating. The deposited films were analysed and characterised using scanning electron microscopy, X-ray powder diffraction, variable temperature UV/Vis/NIR spectroscopy, X-ray photoelectron spectroscopy, glow discharge photoelectron emission spectroscopy and contact angle measurements. Compared to bare VO₂ films, the bilayer films exhibit superior thermochromic properties, with dramatic increases in the visible light transmittance (T_{vis}), integrated luminous transmittance (T_{lum}) and solar modulation (ΔT_{sol}). The thermochromic efficiency was also improved in some cases, with a reduction in the hysteresis loop width to *ca.* 10 °C, and a decrease in the transition temperature (T_c), which was as low as 44 °C and 43 °C for VO₂/ZnO and VO₂/SnO₂ films, respectively. The best balance of thermochromic, thermal protection and aesthetic properties was achieved for ZnO coated films, with the VO₂ under-layer deposited at a field strength of 1500 V m⁻¹ under a negative DC bias ($T_c = 47$ °C, $T_{\text{lum}} = 61.6\%$, $T_{\text{vis}} = 68\%$ and $\Delta T_{\text{sol}} = 6\%$).

1. Introduction

Improving the energy efficiency of buildings through smart window glazings, that control the amount and type of radiation transmitted, is viewed as an important consideration not only in the design of new buildings, but also the retrofitting of existing structures.¹ The coating of window glazings with thermochromic materials allows for thermal control of the transmittance of near infrared (NIR) radiation, whilst maintaining good transmittance of visible radiation^{2,3} and can lead to lower energy demand for indoor climate control.

VO₂ is a thermochromic material which changes its optical properties when heated above a critical temperature, T_c , corresponding to the transition from an insulating monoclinic phase to a tetragonal metallic phase.⁴ When applied as a coating, both UV-Vis and IR radiation are readily transmitted below T_c , with a reduction in NIR radiation transmittance above T_c , whilst maintaining high transmission in the UV-Vis region. The application of VO₂ films is limited by the high T_c of VO₂ (68 °C), small NIR transmittance modulation of around 20%, large thermal hysteresis, low visible light transmittance (T_{vis}) and aesthetically unappealing yellow/brown colour.⁵ An ideal smart window coating should have a T_c around room temperature, with minimal hysteresis behaviour, exhibit thermal and mechanical durability and have a T_{vis} value greater than 60%.

While cationic doping of VO₂ can lead to a lowering of T_c , this is often accompanied by an increase in thermal hysteresis. An alternative approach to improving the properties of VO₂ films is to alter their microstructure. Application of electric fields during aerosol assisted chemical vapour deposition (AACVD) has been shown to be an interesting approach to modulating the morphology and improving the thermochromic properties of VO₂ films,⁶⁻⁹ with films exhibiting particle sizes in the order of *ca.* 5-10 nm. However, the small particle sizes result in greater susceptibility to oxidation, with films readily oxidised to V₂O₅ when heated in air, causing loss of thermochromic properties.^{6,10} For practical implementation of VO₂ based thermochromic coatings, a protective layer can ensure long-term durability of the films, whilst improving the aesthetics and in some cases the thermochromic properties of the active layer.^{11,12} Generally, the top-layer should have a high refractive index and show good thermal and chemical stability.

Calculations have shown that the optimal value of the refractive index, n , of an anti-reflective (AR) top layer for VO₂ films is in the range 2.0 to 2.4.¹³ ZnO, SnO₂ and WO₃ are all potential candidates for this purpose. Indeed, pure ZnO and Al doped ZnO have been used as AR layers in thermochromic VO₂ bilayer films produced by sputtering¹⁴⁻¹⁶ and pulsed layer deposition, respectively.¹⁷ The use of WO₃ as an AR top-layer in thermochromic

glazings has rarely been reported. Long *et al.*¹⁸ recently described the production of WO₃/VO₂/WO₃ multilayer films using sputtering methods. The WO₃ top-layer not only provided successful protection of the VO₂ layer, but also led to significant improvements in the thermochromic properties. SnO₂ has only been used to date in thermochromic applications, as a buffer layer to induce epitaxial growth of VO₂ films, where it is found to reduce T_c and hysteresis behaviour.^{19,20}

In the present study we characterise and compare the thermochromic properties of VO₂-based bilayer films with ZnO, WO₃ and SnO₂ top-layers, the latter for the first time as an AR layer in a thermochromic glazing. Using electric field assisted AACVD (ElFi-AACVD) to produce the VO₂ under-layer, films of varying morphology and porosity can be produced,^{6-8,21} which can influence not only the thermochromic properties of the bilayer films, but also the properties of the top-layer.²² The AR top-layers used in this study are found to dramatically improve the thermochromic properties with respect to bare VO₂ films.

2. Experimental

2.1 VO₂-layer deposition

VO₂ under-layers were deposited using ElFi-AACVD for 15 min in a quartz cold walled reactor, as described previously.⁶ Films were deposited on fluorine doped tin oxide (FTO) coated glass substrates (Pilkington) of dimensions 90 mm × 45 mm × 4 mm, which were washed with acetone (97%) and isopropyl alcohol (99%), sonicated in deionized water for 10 min and dried in flowing N₂ prior to use. A 0.1 M solution of VO(acac)₂ (0.384 g, Sigma-Aldrich, 99.99%) in 15 ml of ethanol (Sigma-Aldrich) was used as the VO₂ precursor. Aerosols were formed using an ultrasonic humidifier, with nitrogen (BOC, 99.99%) as a carrier gas, at a flow rate of 1.5 L min⁻¹. The reaction chamber was heated to 440 °C using a graphite block containing a Whatman heating cartridge, with temperature gradients of up to 50 °C between the top plate and the substrate (separated by 1 cm) and the substrate temperature monitored using a Pt–Rh thermocouple. VO₂ films were deposited using three electric field conditions: (1) DC-positive bias, where a positive potential was applied on the bottom plate; (2) DC-negative bias where a negative potential was applied on the bottom plate and (3) AC, where an alternating current was used. The electric field strength used in all cases was 1500 V m⁻¹. The VO₂ coated substrate plates were cut into 2 cm × 2 cm pieces in preparation for top-layer coating.

2.2 Top-layer deposition

All top-layers were deposited by sol-gel spin coating under flowing nitrogen. All precursors were purchased from Sigma-Aldrich and used without further purification.

For ZnO films, zinc-acetate-dihydrate (8.78 g, 98%) was dissolved in 80 ml of isopropyl alcohol (99.9%) and stirred on a hot plate at 60 °C for 5 min to form a milky solution. Ethanolamine (3.7 ml, 98%) was added to the solution dropwise, which gradually became transparent. The solution was stirred at 60 °C for 1 h and then aged at ambient temperature under dark conditions for 48 h before spin coating.²³ A 0.6 µl drop of the aged solution was spun on the VO₂ coated glass substrate at 2000 rpm for 30 s to give a single layer coating. The coated films were then heated to 500 °C at a heating rate of 10 °C min⁻¹ and annealed at this temperature for 1 h under N₂, at a flow rate of 1.5 L min⁻¹.

For SnO₂ top-layers, 8.37 g of SnCl₂·2H₂O (99%) was dissolved in 65 ml of absolute ethanol (99.99%) to form a 0.1 M solution. This solution was placed in a sealed flask and stirred at 74 °C for 5 h. 5.4 ml of glycerine was added (to give a glycerine:solution ratio of 1:12) as a dispersion stabiliser.²⁴ The resulting sol was aged in a closed flask in the dark for 1 day prior to use. Spin coating of a single top-layer on the VO₂ coated glass substrate was carried out at 900 rpm for 6 s, followed by 3000 rpm for 60 s. The films were then heated to 600 °C at a heating rate of 10 °C min⁻¹ and annealed for 2 h under a low N₂ flow rate of 0.1 L min⁻¹.

For WO₃ top layers, 0.0025 mol (7.39075 g) of (NH₄)₁₀(H₂W₁₂O₄₂)·4H₂O (99%) was dissolved in 12 ml of ethylene glycol at room temperature under constant stirring, followed by sonication for 1 h to ensure complete dissolution. To this, 1.0 ml of deionised water and 0.25 g of Triton-X 100 surfactant (99%) were added, and the solution stirred for 3 h at 85 °C. The sol was then cooled in a closed flask and aged for 2 days in the dark.²⁵ Spin coating of a single top-layer on the VO₂ coated glass substrate was carried out at 2000 rpm for 5 s, followed by 3000 rpm for 180 s. The films were then heated to 500 °C at a heating rate of 1 °C min⁻¹ and annealed at this temperature for 1 h under N₂, at a flow rate of 0.2 L min⁻¹.

Table 1 summarises the films produced and their deposition parameters. Bilayer samples are denoted *VMcond*, where V represents the VO₂ bottom-layer; *M* = Z, S or W, representing the top-layer of ZnO, SnO₂ or WO₃, respectively and *cond* denotes the voltage conditions used in the deposition of the VO₂ bottom layer, with values of 0, dc+15, dc-15 and ac15 indicating zero voltage, +15 V DC bias, -15 V DC bias and 15 V AC, respectively.

2.3 Materials Characterisation

For characterisation, samples were cut into 1 cm² pieces. All samples were stored under dark conditions. Sample adhesion was tested using the standard Scotch tape test, as well as attempted abrasion using tissue paper and brass and steel styli.

Optical measurements were recorded using a Perkin Elmer Lambda 950 UV-Vis spectrometer over the wavelength range 300–2500 nm, in steps of 10 nm, with an air spectral background. Thermochromic properties were initially analysed by heating the samples directly on a hotplate from room temperature up to ~100 °C. For hysteresis measurements, samples were heated in steps of 5 °C using a bespoke sample holder/heater monitored with an R-type thermocouple and spectra recorded on heating and cooling. The transmittance modulation (ΔT) was calculated as the difference in percentage transmittance (% T) between cold and hot states:

$$\Delta T(\%) = \%T_{\text{cold}} - \%T_{\text{hot}} \quad (1)$$

The wavelength integrated optical properties, as characterised by the luminous transmittance (T_{lum} , 380 ≤ λ ≤ 780 nm) and solar transmittance (T_{sol} , 280 ≤ λ ≤ 2500 nm), were calculated using:

$$T_i = \frac{\int \varphi_i(\lambda) T(\lambda) d\lambda}{\int \varphi_i(\lambda) d\lambda} \quad (2)$$

where $T(\lambda)$ is the transmittance at wavelength λ , i denotes luminous or solar radiation, $\varphi_{\text{lum}}(\lambda)$ is the photopic spectral sensitivity of the light-adapted eye (CIE (2008) physiologically-relevant 2-deg $V(\lambda)$ luminous efficiency functions) and φ_{sol} is the solar irradiance spectrum for air mass 1.5, corresponding to the sun standing 37° above the horizon (ASTM G173-03 reference spectrum, direct radiation + circumsolar). Thus, the solar transmittance modulation (ΔT_{sol}) can be calculated by substitution of the T_{sol} values (from equation 2) into equation 1.

Scanning electron microscopy (SEM) was performed using an FEI Inspect F Field Emission SEM at an accelerating voltage of 10 keV and spot size of 3 nm. X-ray powder diffraction (XRD) measurements were made on a PANalytical X'Pert Pro diffractometer in glancing angle ($\alpha = 3^\circ$) mode, using Ni filtered Cu-K α radiation ($\lambda = 1.5418 \text{ \AA}$). The diffraction patterns were collected over the 2θ range 10–70°, with a step size of 0.033° and an effective count time of 1.7 s per step. Contact angles were measured on a Goniometer Kruss DSA100 drop shape analyser and the contact angles measured directly from digital images.

Elemental depth profile analysis was achieved by pulsed radio frequency glow discharge optical emission spectroscopy (RF-GDOES) using a Horiba Scientific GD Profiler 2 analyser. The pulsed-RF (13.56 MHz) sputtering was carried out at 500 Pa, 20 W with a pulsing frequency of 3000 Hz and a duty cycle of 0.25. The analysis spot size corresponds to the anode size, which is 4 mm in diameter. In GDOES the plasma has a double role, it firstly sputters the surface of the sample to be analyzed and secondly excites the sputtered species.²⁶ The de-excitation of the excited species leads to the emission of a characteristic light which is recorded using an optical spectrometer.²⁷ All elements are measured simultaneously and independently. Elemental profiles are therefore presented as an intensity as a function of sputtering time.

X-ray photoelectron spectroscopy (XPS) measurements were performed using a VG Scientific ESCALAB-210 spectrometer, with Al-K α non-monochromated radiation (1486.6 eV; 300 W) as the excitation source. The pressure during analysis was 5.0×10^{-9} mbar. The binding energies of the target elements (V 2*p*, Zn 2*p*, Sn 3*d*, W 4*f* and 5*p*) were determined at a pass energy of 25 eV, using the binding energy of carbon (C 1*s*: 284.8 ± 0.2 eV) as a reference. A Shirley background²⁸ subtraction was applied to obtain the XPS signal intensity. Data were corrected for surface charging effects, prior to fitting using an asymmetric Gaussian/Lorentzian function.

3. Results and Discussion

3.1 Physical Properties

The bare VO₂ films deposited by EFi-AACVD could not be wiped away with blue towel, and passed the scotch tape test, as previously observed.²⁹ Films could not be scratched with a brass stylus, however they could be damaged using a scalpel or a steel stylus. All of the the bilayer films of VO₂ with ZnO, SnO₂ and WO₃ exhibited stronger adherence to the substrate, compared to bare VO₂ films as determined by the scotch-tape test and were resistant to damage from both a scalpel and a steel stylus. The results suggest the bilayer films are likely to show improved durability.

The bare VO₂ films showed characteristic translucency and were brown in colour.⁸ All of the bilayer films were lighter in colour compared to the bare VO₂ films and showed good transparency (Fig. 1). Amongst the three types of bilayer films, the most aesthetically acceptable appearance was obtained with a ZnO top-layer (Fig. 1a), where the film was homogeneous in colour and translucent. The SnO₂ top-layer also improved the colour to some

extent, however this was not entirely homogeneous (Fig. 1b), with both dark and light regions evident. The WO_3 top-layer gave the films a homogeneous light-yellow colour (Fig. 1c). The results are encouraging for potential use of these films in window glazings.

3.2 Depth Profile Analysis

Fig. 2 shows selected RF-GDEOS elemental profiles for representative films. The technique, which involves sputtering the surface of the films with Ar^+ ions and measurement of the emitted light from the ejected elements in the resulting plasma, allows for a qualitative analysis of the different layers of the films as a function of sputtering time, which is correlated to the depth.^{26,27} For the ZnO coated films, Zn is clearly evident in the first stage of sputtering and tails off quickly as the V peak grows, corresponding to the interface between the top- and under- layers. At longer sputtering times, as the V peak diminishes, a peak corresponding to Sn, associated with the FTO coated substrate, emerges. Similar results are seen for the WO_3 and SnO_2 coated films, with those for the SnO_2 coated films showing a bimodal distribution of Sn between the top-layer and substrate. The results confirm successful coating of the films and preservation of the layer structure post-annealing.

3.3 Crystallographic Analysis

The X-ray powder diffraction patterns of the bilayer films are shown in Fig. 3. For each type of top-layer different additional diffraction peaks appear. The patterns of the ZnO coated films (Fig. 3a) are dominated by peaks from the FTO substrate (cassiterite, JCPDS # 41-1445). For the sample with the VO_2 under-layer prepared at zero field (VZ0), weak peaks are evident at 31.8° , 34.3° and 36.2° 2θ , corresponding to the (100), (002) and (101) reflections of ZnO (JCPDS # 36-1451). A weak peak at around 30.1° 2θ is assigned to the tetragonal phase of VO_2 (JCPDS # 42-876). These ZnO and VO_2 peaks are observed in both the VZdc+15 and VZdc-15 samples, but for VZac15 only the FTO peaks are visible.

The XRD patterns of the VO_2/SnO_2 films are shown in Fig. 3b. As expected, the patterns are dominated by that of cassiterite, but comparison with the VO_2/ZnO films suggests that most of this is from the FTO substrate. For the VSdc+15 sample, a weak peak at 42.5° 2θ is seen, associated with the (111) reflection of monoclinic VO_2 (JCPDS # 33-1441). Another peak at 20.1° 2θ can be assigned to the shcherbinaite form of V_2O_5 . For VSdc-15, further peaks evident at around 12.2° , 18.5° , and 29.0° 2θ are attributable to the orthorhombic form of V_2O_5 (JCPDS # 45-1074). The appearance of V_2O_5 in these films is indicative of partial

oxidation, suggesting incomplete protection of the VO₂ under-layer by the SnO₂ top-layer and is consistent with the colour inhomogeneity seen in the optical image in Fig.1b. For the sample where the VO₂ under-layer was prepared in an AC field (VSac15), only those peaks attributable to cassiterite are seen, as for the analogous ZnO coated film (VZac15).

The XRD patterns of the VO₂/WO₃ bilayer films are shown in Fig. 3c. Unlike the other bilayer films studied, those with a WO₃ top-layer exhibit strong diffraction peaks from the top-layer, due to the greater X-ray scattering power of tungsten, as well as better crystallinity. All patterns show strong peaks between 23.0° to 24.0°, which are assigned to the (200), (020) and (002) reflections of monoclinic WO₃ (JCPDS # 43-1035). Other peaks from this phase extensively overlap with those from the FTO substrate. In fact, the structural distortions of the corner-sharing array of WO₆ octahedra in WO₃ are quite complex and make definitive assignments of WO₃ phases from XRD data alone rather difficult.³⁰ Therefore, assignment to the monoclinic phase is tentative. In the diffraction pattern for the VW0 sample, only peaks arising from WO₃ and FTO were discernible. In the XRD pattern for the VWdc+15 sample, the WO₃ peaks are broadened compared to those in the pattern for the VW0 sample. A weak peak at around 27.4° 2θ is observed, attributable to tetragonal VO₂ (JCPDS # 44-253). For the film with the bottom layer prepared under negative DC bias, the pattern of broadened WO₃ peaks between 23.0 and 24.0 changes somewhat, suggesting a change in the WO₃ phase distribution. Indeed, the diffraction patterns for δ-WO₃ and monoclinic γ-WO₃ phases are very similar and these phases are reported to co-exist at room temperature, depending on sample preparation conditions.³¹ The pattern for the VWac15 sample is similar to that for VWdc+15, but in this case there is some evidence for a weak peak at around 27.4° 2θ, indicative of VO₂, although the weakness of the peak prevents unambiguous distinction between the tetragonal and monoclinic forms.

3.4 Surface Morphology

SEM images of selected films are shown in Fig. 4, with images of all films given in the supporting information as Figs. S1 to S4. The morphologies of the ZnO top-layers of the different VO₂/ZnO bilayer films, showed only subtle differences attributable to differences in the VO₂ under-layer morphology (Fig. S1). The ZnO covered films (Fig. S2) exhibited complete surface coverage, provided by smaller nanoparticles, with particle sizes in the range of ~5-20 nm. The surface of the VZdc-15 film (Fig. 4b) exhibited some agglomeration of particles and some cracking compared to the other films, due to loss of the volatile components during

calcination. This sample corresponded to the film with the highest porosity and irregularity in the VO₂ under-layer (Fig. 4a). In comparison to the VO₂/ZnO films, SnO₂ coated films showed a more significant difference in the surface morphology between samples (Fig. S3). For samples where the VO₂ under-layers were produced under DC or zero electric fields, the SnO₂ layers consisted of rounded clusters made up of smaller nanoparticles (*ca.* 20 nm), with uniform coverage. The cluster size and porosity increased in the order VS0 < VSdc+15 < VSdc-15, with average cluster sizes of 40, 80 and 90 nm, respectively. A significant difference in the surface morphology was observed for the VSac15 film, compared to the other films. Its surface consisted of larger, inverted plate-like structures aligned randomly. The coverage was less uniform, with high porosity, revealing the VO₂ under-layer in some places. All VO₂/WO₃ films were fairly featureless, homogeneous and compact. The surface morphology was rougher for films produced under electric fields than for the film produced at zero field. A scattering of smaller particles on the surface of the VWdc-15 (Fig. 4d) is observed as well as irregular cracking in all the WO₃ coated films, due to evaporation of excess solvent and shrinkage.

3.5 Thermochromic Properties of the Films

UV-Vis-NIR spectroscopy was used in transmission mode in order to determine the thermochromic and optical properties of the films. The transmittance spectra for representative bilayer films at 25 °C, and 80 °C, which lie below and above T_c , respectively, are shown in Fig. 5, with spectra for all films given in the supporting information as Figs. S5 to S7. All films exhibited reversible thermochromic colouration over three cycles, confirming the effectiveness of the protective top-layers. In most cases, the highest NIR transmittance modulation was obtained at around 1300 nm, above which the transmittance properties are dominated by the FTO substrate. Therefore, all transmittance values are reported at this wavelength. Table 2 summarises the transmittance modulation and visible light transmittance values for all the bilayer films in the present study. For the ZnO coated films (Fig. S5), similar levels of NIR transmittance modulation (ΔT) of around 20% were observed in all films apart from VZac15, which showed about half the NIR transmittance modulation of the other films. These ΔT values of between 10-20% are comparable to those reported for bare VO₂ films produced under electric fields.^{6,7,21,32} Additionally, the highest visible light transmittance value was obtained for the VZdc-15 sample, with a value of 68%, which is higher than that of bare VO₂ films produced by EIFi-AACVD (*ca.* 30% - 50%).^{6,7,21,22} This high visible light transmittance is evident in Fig. 1a, where the image below the ZnO coated film is clearly seen. Integrated luminous transmittance and solar modulation values for the VO₂/ZnO bilayer films

are given in Table 2. T_{lum} values were in the range of 45.9 to 61.6 %, where the highest T_{lum} was obtained from the VZdc-15 film. ΔT_{sol} values for the VO₂/ZnO bilayer films varied between 4.9 and 9.1%, where the VZdc+15 sample exhibited the highest value. Compared to VO₂/ZnO films produced by other methods the films reported here show comparable ΔT_{sol} , but higher T_{lum} values.^{15,16}

In the case of SnO₂ coated films (Fig. S6), where VO₂ under-layers were deposited under DC fields, significantly better transmittance modulation is observed, than in those with under-layers deposited in zero field or AC fields. As in the case of the ZnO coated films, the highest NIR ΔT value (25%) was obtained from the film with a VO₂ under-layer deposited under a negative DC bias, where the under-layer had the highest porosity. As with ZnO, SnO₂ served as an AR layer, causing a marked increase in T_{vis} and T_{lum} , with maximum values of 67% and 55.9%, respectively for the VSdc-15 film (Table 2). ΔT_{sol} values for the VO₂/SnO₂ bilayer films varied between 1.0 and 4.3%. While for the VS0 film, a significant reduction in ΔT_{sol} is observed with respect to the bare VO₂ film, for the other films little or no reduction is observed and in the case of the VSac15 film a significant increase in ΔT_{sol} is seen.

Apart from VWac15, all other VO₂/WO₃ bilayer films exhibited high ΔT values of *ca.* 30%, which is higher than those of bare VO₂ films prepared by ElFi-AACVD.⁸ Interestingly, for VWdc+15 and VWac15 samples, near zero NIR light transmittance was obtained at 80 °C, indicating the possibility of blocking virtually all NIR radiation. The highest T_{vis} value was obtained for the film where the bottom layer was deposited in the absence of an electric field (VW0), with those for the other films in the range 45–55 %, significantly less than commercially available systems (*ca.* 65%).³² The ΔT_{sol} values are all increased for the VO₂/WO₃ bilayer films compared to bare VO₂ films, with the highest value obtained for the VW0 sample (9.2%). The values for T_{lum} are reduced with respect to the bare VO₂ films for films where the bottom layer was prepared under DC bias, but virtually the same for the other two films. The highest observed T_{lum} value is higher than those previously reported on the WO₃/VO₂/WO₃ sandwich structures¹⁸ and bilayer films with other AR coatings.^{10,17,33}

3.6 Thermochromic Efficiency of the Films

The thermochromic efficiency of films was assessed by examining the reversibility of transmittance modulation in thermal cycling. The width of the resulting hysteresis loop represents a measure of the thermochromic efficiency, while the mid-point of the loop represents the critical transition temperature (T_c). For bare VO₂ films, variations in the hysteresis loop width have previously been correlated to the particle size and morphology of

the VO₂ layer.³⁴⁻³⁷ VO₂ films which consist of smaller nanoparticles with well-defined shapes, have large interfacial energies, which can result in a desired reduction in T_c , but also tends to lead to undesirable larger hysteresis widths. In the present case only small reductions in T_c (66-61 °C), compared to the bulk solid value of 68 °C, are seen in the bare VO₂ films produced in electric fields, consistent with previous studies.²² As seen in Table 2, almost all bilayer films showed a significant reduction in T_c compared to that of bare VO₂ films, with the exception of the two SnO₂ coated films with VO₂ under-layers deposited under DC fields. In contrast, the SnO₂ coated film with a bottom layer deposited in an AC field showed the lowest T_c value (43 °C) of all the films investigated. Hysteresis loops for bilayer films with VO₂ under-layers prepared under negative DC bias are shown in Fig. 6 as representative examples, with the remainder given in the supporting information as Figs. S8 to S10. The widest hysteresis loop for the films in Fig. 6 is shown by the WO₃ coated film, with that for the SnO₂ coated film the narrowest, which is also the narrowest width for all studied films; however, this film also had a high T_c value as seen in Table 2.

The observed reduction of T_c in some of the films can be explained by two possible mechanisms. For VO₂ films, it is known that small deviations in stoichiometry, as a result of redox processes during annealing, can result in a reduction of T_c .^{38,39} These changes in stoichiometry can be regarded as doping VO₂ with aliovalent vanadium cations and hence are not fundamentally different to doping by cations of different metals. Indeed, Zn,⁴⁰ Sn,⁴¹ and W^{42,43} as dopants have all been shown not only to reduce the T_c of VO₂ films, but also to improve the T_{lum} and NIR/solar modulation values. Since the VO₂ under-layers in the present study showed an irregular and porous surface morphology, formed of nanoparticles, diffusion of Zn²⁺, Sn⁴⁺ and W⁶⁺ ions from the top-layers during the annealing step is a likely occurrence. These dopants can result in changes in the bandgap,^{44,45} a reduction in the crystallite size⁴⁶ or in the case of doping by subvalent cations, introduction of oxygen vacancies. Substitution of vanadium in VO₂ leads to interruption of the zigzag chains of V-V pairs, characteristic of the low-temperature phase, resulting in a lower energy requirement for the monoclinic to tetragonal phase transition and hence a lowering of T_c .⁴⁷ Similar observations have been made in multilayer films of VO₂ with TiO₂,²² WO₃,³⁸ and SiO₂,⁴⁸ where the VO₂ under-layer had a porous irregular morphology. Lee *et al.*⁴⁹ have reported that Sn doping into VO₂ raises T_c and in the case of the SnO₂ coated films in the present study, the high T_c values obtained for films with under-layers deposited under DC field, suggest that some diffusion of Sn⁴⁺ cations from the top-layer to the under-layer may occur.

Another potential factor is the existence of internal and thermal stresses between the layers in the bilayer films. VO₂ deposition on buffer layers of ZnO,²⁰ SnO₂^{19,20} and WO₃¹⁸ have resulted in heteroepitaxial VO₂ films with reduced T_c values attributed to strain effects. In a similar way, the presence of lattice strain caused by a metal oxide top-layer on a VO₂ under-layer has been reported in TiO₂/VO₂ bilayer films^{22,50} and this type of strain induced effect may well contribute to the T_c reductions seen in the present work.

Taking into account all measures of thermochromic performance discussed above, whilst there were examples of all three types of coatings that exhibited good properties, the ZnO coated films showed a better balance of properties, with the VZdc-15 film the best of these, including a high T_{lum} of 61.6%, good NIR transmittance modulation of 20%, solar modulation of 6.0%, and a low T_c of 47 °C. In addition, the ZnO coated films showed the best aesthetics, with a homogeneous translucent colour.

3.7 Thermal Protection

The thermochromic behaviour was reproducible over three cycles of heating and cooling up to 80 °C, indicating the effectiveness of ZnO, SnO₂ and WO₃ as protective top-layers. In order to assess the extent of thermal oxidation protection offered by the top-layers, previously cycled bilayer films were examined by XPS.

Fig. 7 shows XPS spectra for selected samples with binding energies summarised in Table 3 (data could not be collected on the VZac15 film). Other spectra are given in the supporting information as Figs S11 to S13. Characteristic doublets for Zn 2p_{3/2} and 2p_{1/2}, Sn 3d_{5/2} and 3d_{3/2} and W 4f_{7/2} and 4f_{5/2} electrons are evident, with the respective binding energies in good agreement with literature values,⁵¹⁻⁵³ confirming deposition of the SnO₂ and WO₃ top layers in their expected oxidation states of 4+ and 6+, respectively. The vanadium spectra show the characteristic 2p_{3/2} 2p_{1/2} doublet, but are complicated by the presence of O 1s satellite peaks at around 517.7 and 519.2 eV (*ca.* 10 and 12 eV below the strong O1s peak at *ca.* 530 eV). The V 2p_{3/2} binding energy varies from 516.5 to 516.8 eV in the ZnO coated films and is comparable to values for VO₂ previously reported.⁵⁴ In the case of the SnO₂ coated films there is a slightly higher average V 2p_{3/2} binding energy across the different films, varying from 516.8 to 516.9 eV, which suggests that while there is some oxidation, as evidenced in the X-ray diffraction data (Fig. 3), vanadium is predominantly in the 4+ oxidation state. This is consistent with the more porous morphology of the SnO₂ coated films (Fig. 4). Comparison of the V 2p_{3/2} binding energies in the WO₃ coated films of 516.8 to 517.1 eV with that for V₂O₅ of 517.26 eV,⁵⁵ suggests a greater degree of oxidation of

vanadium to the 5+ state in these films. The fact that no evidence of V_2O_5 was found in the X-ray diffraction data for these films is probably due to the greater X-ray scattering power of tungsten, leading to domination of the patterns by tungsten oxide. The results indicate that the ZnO coated films offer the best thermal protection to oxidation. However, since all films showed reversible thermochromic properties over at least three cycles of heating and cooling, all coatings give some degree of protection.

3.8 Contact Angle Measurements

Fig. 8 shows images of water droplets on the surfaces of the studied bilayer films. Low contact angles are found for several films. These are correlated with the morphology of the top-layer, with the porous SnO_2 coated films showing very low contact angles, *i.e.* greater wettability. For the films with VO_2 under-layers produced in the absence of an electric field, the WO_3 coated films show the lowest contact angle. For films with VO_2 under-layers produced under electric fields, the ZnO and SnO_2 coated films all showed a reduction in contact angle, reflecting small changes in the morphology of the top-layer, caused by changes in that of the under-layer. The low contact angle of the VW0 film is reflected in the other WO_3 coated films, with that for the VWdc+15 film showing an even lower contact angle of 16.2° .

4. Conclusions

Thermochromic bilayer thin films of VO_2 with ZnO, SnO_2 and WO_3 top-layers were fabricated by a combination of electric field assisted AACVD and sol-gel spin coating onto FTO coated glass substrates. Introduction of the top layers of ZnO and SnO_2 over VO_2 , dramatically increased the visible light transmittance to *ca.* 65-70%, whereas the highest increase of the NIR transmittance modulation (ΔT_{1300}) of 30% was obtained with the WO_3 top-layer coatings. The top-layer coatings also caused a noticeable decrease in T_c . The lowest T_c values of $44^\circ C$ and $43^\circ C$ were obtained for VO_2/ZnO and VO_2/SnO_2 films, where the VO_2 under-layers were both produced under AC fields. It was found that the presence of an electric field during deposition of the VO_2 under-layer could lead to a marked change in the microstructure of the top-layers, particularly improving the thermochromic properties and reducing water contact angles, without application of UV light.

These bilayer structures showed notable improvement of optical properties compared to the bare VO₂ films, indicating that the metal oxide top layers used in this study can be effectively used as the AR layer while working as a protective layer that can prevent the oxidation of VO₂ layer as well. Additionally, these top layers improve the aesthetic appearance of the glazing and visible light transmittance, as well as providing enhanced wetting behaviour. While all the types of top-layer coatings offered a degree of thermal protection and some improvement in thermochromic properties, the best balance of aesthetic, thermal protection and thermochromic properties was achieved for the VZdc-15 film, which exhibited values of $T_c = 47$ °C, $T_{lum} = 61.6\%$ and $\Delta T_{sol} = 6\%$. The ZnO coated films, in particular, have potential for application in thermochromic glazing.

Conflicts of Interest

There are no conflicts of interest to declare.

Acknowledgements

IT gratefully thanks the Turkish Higher Research Council (TUBITAK) for a BIDEB 2213 PhD scholarship. IP and CS acknowledge funding from by ERC grant IntelGlazing and EENSULATE. Dr. R. M. Wilson at Queen Mary University of London is thanked for his help in X-ray powder diffraction data collection.

References

1. T. C. Chang, X. Cao, S. H. Bao, S. D. Ji, H. J. Luo and P. Jin, *Adv. Manuf.*, 2018, **6**, 1-19.
2. A. L. Anderson, S. Chen, L. Romero, I. Top and R. Binions, *Buildings*, 2016, **6**, 37.
3. C. G. Granqvist, Y. X Ji, J. Montero and G. A. Niklasson, *J. Phys. Conf. Ser.*, 2016, **764**, 012002.
4. C. Liu, S. Wang, Y. Zhou, H. Yang, Q. Lu, D. Mandler, S. Magdassi, C. Y. Tay and Y. Long, *J. Alloys Compd.*, 2018, **731**, 1197–1207.
5. M. E. A. Warwick and R. Binions, *J. Mater. Chem. A*, 2014, **2**, 3275.
6. M. E. A. Warwick and R. Binions, *J. Nanosci. Nanotechnol.*, 2011, **11**, 1–6.
7. M. E. A. Warwick, R. Smith, N. Furlan, J. Crane and R. Binions, *ECS Trans.*, 2010 **28**, 1–13.
8. M. E. A Warwick and R. Binions, R., *Sol. Energy Mater. Sol. Cells*, 2015, **143**, 592–

- 600.
9. N. R. Mlyuka, G. A. Niklasson and C. G. Granqvist, *Phys. Status Solidi Appl. Mater. Sci.*, 2009, **206**, 2155–2160.
 10. C. Liu, N. Wang and Y. Long, *Appl. Surf. Sci.*, 2013, **283**, 222–226.
 11. Y. X. Ji, S. Y. Li, G. A. Niklasson and C. G. Granqvist, *Thin Solid Films*, 2014, **562**, 568–573.
 12. Y. X. Ji, G. A. Niklasson and C. G. Granqvist, *J. Phys. Conf. Ser.*, 2014, **559**, 12005.
 13. G. Xu, P. Jin, M. Tazawa, and K. Yoshimura, *Sol. Energy Mater. Sol. Cells*, 2004, **83**, 29–37.
 14. A. Srivastava, T. S. Heng, S. Saha, B. Nina, A. Annadi, N. Naomi, Z. Q. Liu, S. Dhar, Ariando, J. Ding and T. Venkatesan, *Appl. Phys. Lett.*, 2012, **100**, 241907.
 15. H. Zhou, J. Li, S. Bao, J. Li, X. Liu and P. Jin, *Appl. Surf. Sci.*, 2016, **363**, 532–542.
 16. E. Gagaoudakis, E. Aperathitis, G. Michail, M. Panagopoulou, D. Katerinopoulou, V. Binas, Y.S. Raptis and G. Kiriakidis, *Sol. Energy*, 2018, **165**, 115–121.
 17. L. Kang, Y. Gao, H. Luo, J. Wang, B. Zhu, Z. Zhang, J. Du, M. Kanehira and Y. Zhang, *Sol. Energy Mater. Sol. Cells*, 2011, **95**, 3189–3194.
 18. S. Long, H. Zhou, S. Bao, Y. Xin, X. Cao and P. Jin, *RSC Adv.*, 2016, **6**, 106435–106442.
 19. M. Panagopoulou, E. Gagaoudakis, E. Aperathitis, I. Michail, G. Kiriakidis, D. Tsoukalas and Y.S. Raptis. *Thin Solid Films*, 2015, **594**, 310–315.
 20. H. Koo, L. Xu, K. E. Ko, S. Ahn, S. H. Chang and C. Park, *J. Mater. Eng. Perform.*, 2013, **22**, 3967–3973.
 21. A. J. T. Naik, C. Bowman, N. Panjwani, M. E. A. Warwick and R. Binions, *Thin Solid Films*, 2013, **544**, 452–456.
 22. I. Top, R. Binions, M. E. A. Warwick, C. W. Dunnill, M. Holdynski and I. Abrahams *J. Mater. Chem. C*, 2018, **6**, 4485–4493.
 23. S. Chen, M. E. A. Warwick and R. Binions, *Sol. Energy Mater. Sol. Cells*, 2015, **137**, 202–209.
 24. S. Gong, J. Liu, J. Xia, L. Quan, H. Liu and D. Zhou, *Mater. Sci. Eng. B Solid-State Mater. Adv. Technol.*, 2009, **164**, 85–90.
 25. H. Zhang, P. Yilmaz, J. O. Ansari, F. F. Khan, R. Binions, S. Krause and S. Dunn, *J. Mater. Chem. A*, 2015, **3**, 9638–9644.
 26. J. Pisonero, *Anal. Bioanal. Chem.*, 2013, **405**, 5655–5662.
 27. M. R. Winchester and R. Payling, *Spectrochim. Acta - Part B At. Spectrosc.*, 2004, **59**,

- 607–666.
28. D. A. Shirley, *Phys. Rev. B*, 1972, **5**, 4709–4714.
 29. D. Louloudakis, D. Vernardou, E. Spanakis, N. Katsarakis and E. Koudoumas, *Phys. Procedia*, 2013, **46**, 137–141.
 30. M. B. Johansson, G. A. Niklasson, L. Österlund, *J. Mater. Res.*, 2012, **27**, 3130–3140.
 31. A. G. S. Filho, J. M. Filho, V. N. Freire, A. P. Ayala, J. M. Sasaki, P. T. C. Freire, F. E. A. Melo, J. F. Juliao and U. U. Gomes, *J. Raman Spectrosc.*, 2001, **32**, 695–699.
 32. M. E. A. Warwick, I. Ridley and R. Binions, *Sol. Energy Mater. Sol. Cells*, 2016, **157**, 686–694.
 33. H. Koo, D. Shin, S. H. Bae, K. E. Ko, S. H. Chang and Chan Park, *J. Mater. Eng. Perform.*, 2013, **23**, 402–407.
 34. H. Zhang, Z. Wu, D. Yan, X. Xu and Y. Jiang, *Thin Solid Films*, 2014, **552**, 218–224.
 35. H. Zhang, Z. Wu, X. Wu, W. Yang and Y. Jiang, *Vacuum*, 2014, **104**, 47–50.
 36. J. Y. Suh, R. Lopez, L. C. Feldman and R. F. Haglund, *J. Appl. Phys.* 2004, **96**, 1209–1213.
 37. H. Zhang, Z. Wu, Q. He and Y. Jiang, *Appl. Surf. Sci.*, 2013, **277**, 218–222.
 38. S. Zhang, I. S. Kim and L. J. Lauhon, *Nano Lett.* 2011, **11**, 1443–1447.
 39. J. Zheng, S. Bao and P. Jin, *Nano Energy*, 2015, **11**, 136–145.
 40. M. Jiang, S. Bao, X. Cao, Y. Lia, S. Li, H. Zhou, H. Luo and P. Jin, *Ceram. Int.* 2014, **40**, 6331–6334.
 41. Y. Zhang, J. Zhang, X. Zhang, C. Huang, Y. Zhong and Y. Deng, *Mater. Lett.*, 2013, **92**, 61–64..
 42. L. Hu, H. Tao, G. Chen, R. Pan, M. Wan, D. Xiong and X. Zhao, *J. Sol-Gel Sci. Technol.*, 2016, **77**, 85–93..
 43. Y. Wu, L. Fan, W. Huang, S. Chen, S. Chen, F. Chen, C. Zou and Z. Wu, *Phys. Chem. Chem. Phys.*, 2014, **16**, 17705.
 44. J. B. Goodenough, *J. Solid State Chem.*, 1971, **3**, 490–500.
 45. S. Y. Li, N. R. Mlyuka, D. Primetzhofer, A. Hallen, G. Possnert, G. A. Niklasson, and C. G. Granqvist. *Appl. Phys. Lett.*, 2013, **103**, 161907.
 46. C. Piccirillo, R. Binions and I. P. Parkin, *Thin Solid Films*, 2008, **516**, 1992–1997.
 47. X. Cao, N. Wang, S. Magdassi, D. Mandler and Y. Long, *Sci. Adv. Mater.*, 2014, **6**, 558–561.
 48. J. Zhang, J. Wang, C. Yang, H. Jia, X. Cui, S. Zhao, *Sol. Energy Mater. Sol. Cells*, 2007, **162**, 134–141.

49. M. H. Lee, M. G. Kim and H. K. Song, *Thin Solid Films*, 1996, **290–291**, 30–33.
50. M. J. Powell, R. Quesada-Cabrera, A. Taylor, D. Teixeira, I. Papakonstantinou, R. G. Palgrave, G. Sankar and I. P. Parkin, *Chem. Mater.*, 2016, **28**, 1369–1376.
51. R. Al-Gaashani, S. Radiman, A. R. Daud, N. Tabet and Y. Al-Douri, *Ceram. Int.*, 2013, **39**, 2283–2292.
52. A. Phukan, R. P. Bhattacharjee and D. K. Dutta, *Adv. Powder Technol.*, 2017, **28**, 139–145.
53. R. Sivakumar, R. Gopalakrishnan, M. Jayachandran and C. Sanjeeviraja, *Smart Mater. Struct.*, 2006, **15**, 877–888.
54. G. Silversmit, D. Depla, H. Poelman, G. B. Marin and R. De Gryse, *J. Electron Spectros. Relat. Phenomena*, 2004, **135**, 167–175.
55. M. C. Biesinger, L. W. M. Lau, A. R. Gerson, and R. S. C. Smart, *Appl. Surf. Sci.*, 2010, **257**, 887–898.

Table 1. Summary of electric field deposition parameters used in the production of bilayer films in the present study.

Sample Name	Voltage type	Field Strength (V m⁻¹)	Films
V0	-	0	VO ₂
Vdc+15	DC (+)	1500	VO ₂
Vdc-15	DC (-)	1500	VO ₂
Vac15	AC	1500	VO ₂
VZ0	-	0	VO ₂ /ZnO
VZdc+15	DC (+)	1500	VO ₂ /ZnO
VZdc-15	DC (-)	1500	VO ₂ /ZnO
VZac15	AC	1500	VO ₂ /ZnO
VS0	-	0	VO ₂ /SnO ₂
VSdc+15	DC (+)	1500	VO ₂ /SnO ₂
VSdc-15	DC (-)	1500	VO ₂ /SnO ₂
VSac15	AC	1500	VO ₂ /SnO ₂
VW0	-	0	VO ₂ /WO ₃
VWdc+15	DC (+)	1500	VO ₂ /WO ₃
VWdc-15	DC (-)	1500	VO ₂ /WO ₃
VWac15	AC	1500	VO ₂ /WO ₃

Table 2. Visible light transmittance (T_{vis}) at 600 nm, transmittance modulation (ΔT) at 1300 nm, integrated luminous (T_{lum}) and solar (T_{sol}) modulations and critical transition temperature measured at 1300 nm (T_c), for the studied bare VO₂ and bilayer films.

Sample	ΔT (%)	T_{vis} (%)	$T_{lum,c}$ (%)	$T_{lum,h}$ (%)	$T_{sol,c}$ (%)	$T_{sol,h}$ (%)	ΔT_{sol} (%)	T_c (°C)
V0*	22	49	46.0	44.7	42.5	34.7	7.7	66
Vdc+15*	16	48	46.5	45.3	40.5	36.3	4.1	61
Vdc-15*	2	50	50.0	48.8	40.7	39.4	1.3	61
Vac15*	20	45	40.0	43.4	32.8	30.0	2.7	61
VZ0	20	54	48.8	46.4	45.6	38.8	6.8	51
VZdc+15	22	55	45.9	43.8	42.2	33.1	9.1	54
VZdc-15	21	68	61.6	60.8	56.6	50.7	6.0	47
VZac15	10	50	44.3	42.8	38.6	33.7	4.9	44
VS0	10	60	53.0	52.7	47.4	44.1	3.3	49
VSdc+15	25	43	28.4	27.7	26.6	22.2	4.3	61
VSdc-15	22	67	55.9	56.3	52.5	51.4	1.0	64
VSac15	10	49	20.3	20.0	22.5	18.2	4.3	43
VW0	30	60	46.6	45.9	44.2	35.0	9.2	51
VWdc+15	30	40	31.7	29.0	30.0	21.3	8.6	51
VWdc-15	30	50	39.6	38.9	37.8	30.5	7.2	51
VWac15	20	49	42.4	41.1	37.4	33.0	4.38	46

*Values for $T_{lum,c}$, $T_{lum,h}$, $T_{sol,c}$, $T_{sol,h}$ and ΔT_{sol} for bare VO₂ films from Top *et al.* ²⁶

Table 3. Binding energies (eV) from XPS spectra for studied bilayer films.

Sample	V $2p_{3/2}$	V $2p_{1/2}$	Zn $2p_{3/2}$	Zn $2p_{1/2}$	Sn $3d_{5/2}$	Sn $3d_{3/2}$	W $4f_{7/2}$	W $4f_{5/2}$
VZ0	516.7	522.0	1021.8	1044.9				
VZdc-15	516.8	521.0	1021.7	1044.8				
VZdc+15	516.5	522.6	1021.8	1045.0				
VS0	516.8	523.4			486.6	495.1		
VSdc-15	516.9	524.1			486.5	494.9		
VSdc+15	516.9	524.1			486.5	494.9		
VSac15	516.9	524.1			486.7	495.2		
VW0	517.0	524.0					35.2	37.3
VWdc-15	517.1	524.2					35.1	37.2
VWdc+15	517.1	524.2					35.2	37.3
VWac15	516.8	523.8					35.1	37.2

Figure captions

Fig. 1. Representative photographs of bilayer films of VO₂ with (a) ZnO (b) SnO₂ and (c) WO₃ top-layers.

Fig. 2. RF-GDOES profiles for representative bilayer films: (a) VZdc-15 (b) VSdc-15 and (c) VWdc-15, where black, red, blue lines and green denote V, Zn, Sn and W, respectively.

Fig. 3. X-ray powder diffraction patterns for bilayer films of VO₂ with (a) ZnO, (b) SnO₂ and (c) WO₃ top-layers. Peaks attributed to cassiterite SnO₂ (*), ZnO (▼), monoclinic-VO₂ (◆), scherbinaitite V₂O₅ (●), orthorhombic V₂O₅ (♥) and WO₃ (■) are indicated.

Fig. 4. Representative SEM images of films with VO₂ layers produced under -15 V DC bias: (a) Vdc-15 (b) VZdc-15 (c) VSdc-15 and (d) VWdc-15. All images were taken at 100000 × magnification.

Fig. 5. Hot and cold UV-Vis-NIR transmittance spectra for representative bilayer films: (a) VZdc-15, (b) VSdc-15 and (c) Vwdc-15, where red and blue lines represent hot and cold stages, respectively.

Fig. 6. Representative NIR transmittance hysteresis plots recorded at 1300 nm for selected bilayer films of VO₂ with ZnO, SnO₂ and WO₃ top-layers. Heating and cooling are indicated by red and blue lines, respectively. The values of T_c are taken as the mid points of the width of the hysteresis, as shown.

Fig. 7. Fitted XPS spectra for representative bilayer films: (a) VZdc-15 V spectrum, (b) VZdc-15 Zn spectrum, (c) VSdc-15 V spectrum (d) VSdc-15 Sn spectrum, (e) VWdc-15 V spectrum and (f) VWdc-15 W spectrum.

Fig. 8. Water contact angle images taken for bilayer films of VO₂/ZnO, VO₂/SnO₂ and VO₂/WO₃.

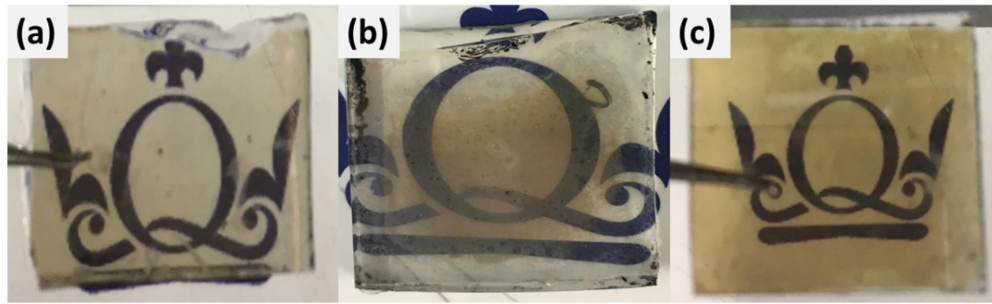


Fig. 1. Representative photographs of bilayer films of VO₂ with (a) ZnO (b) SnO₂ and (c) WO₃ top-layers.

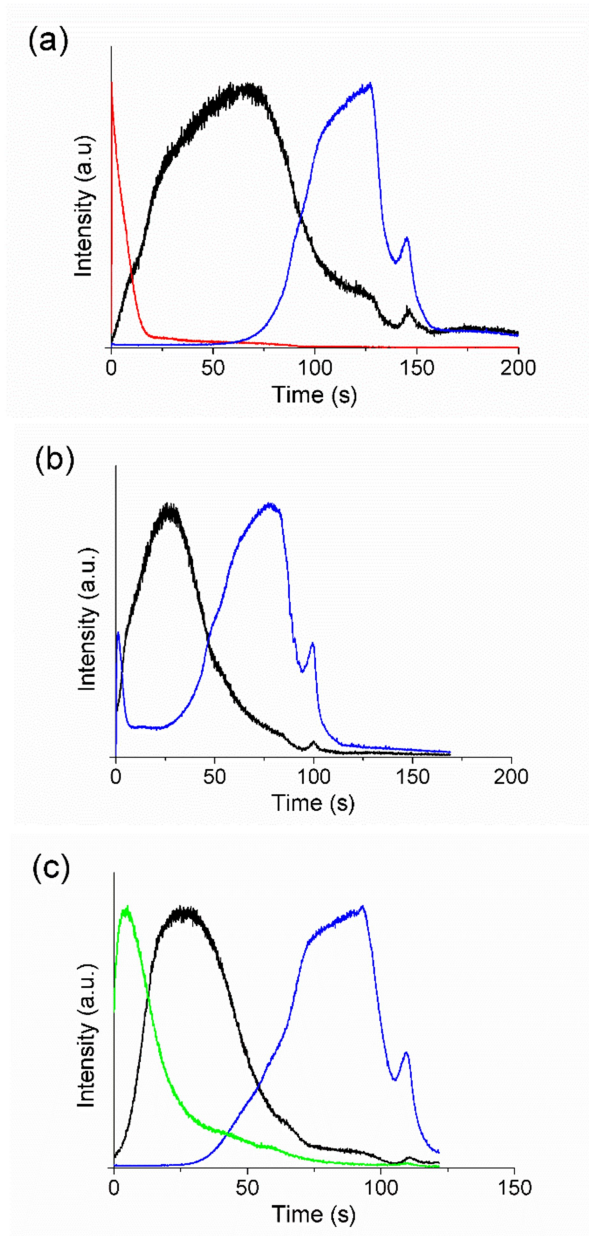
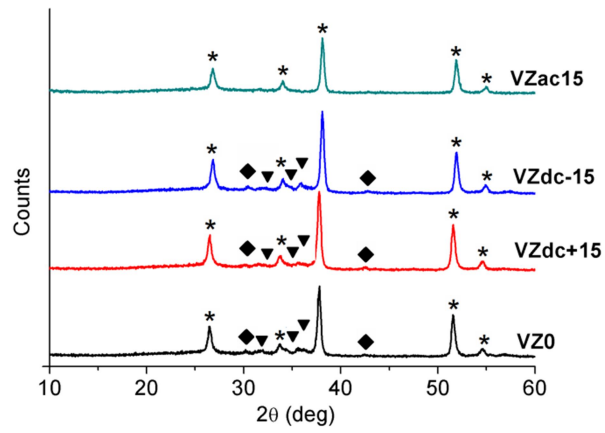
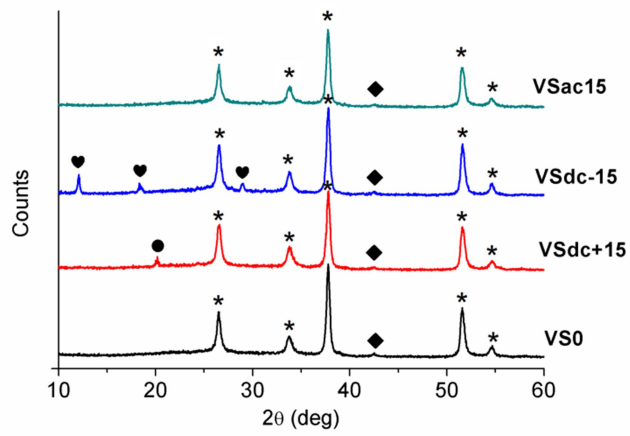


Fig. 2. RF-GDOES profiles for representative bilayer films: (a) VZdc-15 (b) VSdc-15 and (c) VWdc-15, where black, red, blue lines and green denote V, Zn, Sn and W, respectively.

(a)



(b)



(c)

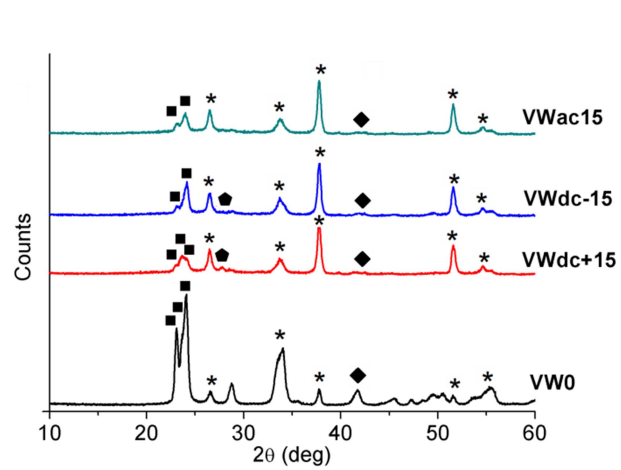


Fig. 3. X-ray powder diffraction patterns for bilayer films of VO₂ with (a) ZnO, (b) SnO₂ and (c) WO₃ top-layers. Peaks attributed to cassiterite SnO₂ (*), ZnO (▼), monoclinic-VO₂ (◆), scherbinaite V₂O₅ (●), orthorhombic V₂O₅ (♥) and WO₃ (■) are indicated.

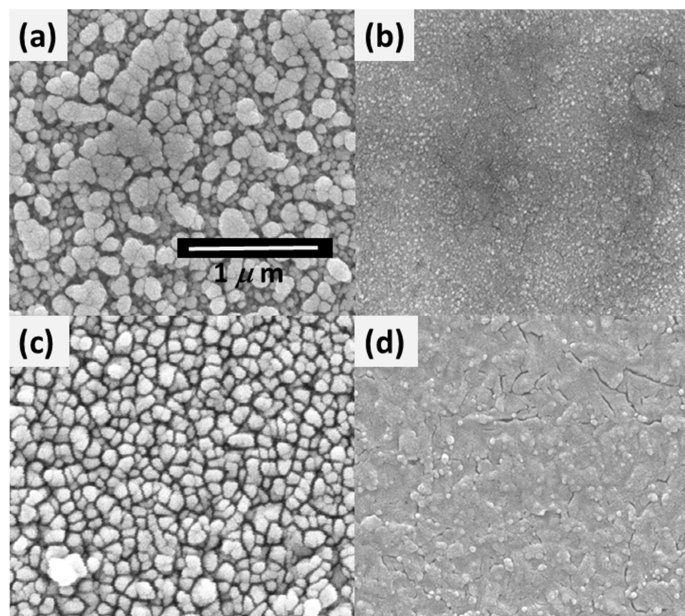


Fig. 4. Representative SEM images of films with VO₂ layers produced under -15 V DC bias: (a) Vdc-15 (b) VZdc-15 (c) VSdc-15 and (d) VWdc-15. All images were taken at 100000 × magnification.

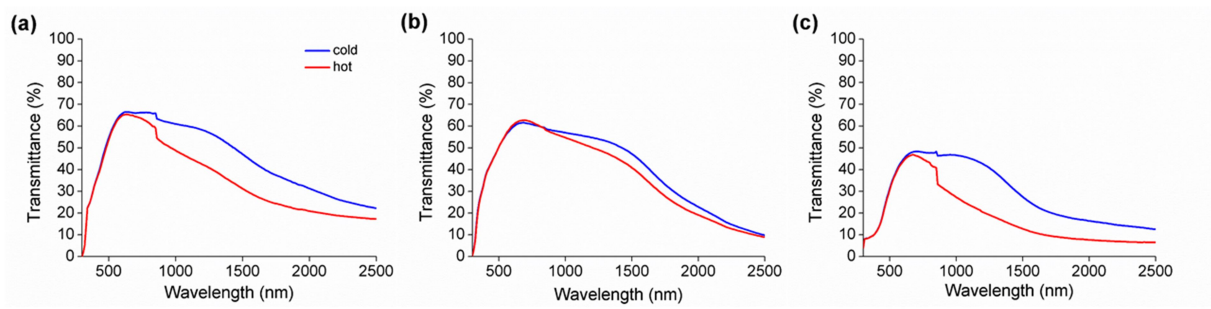


Fig. 5. Hot and cold UV-Vis-NIR transmittance spectra for representative bilayer films: (a) VZdc-15, (b) VSdc-15 and (c) VWdc-15, where red and blue lines represent hot and cold stages, respectively.

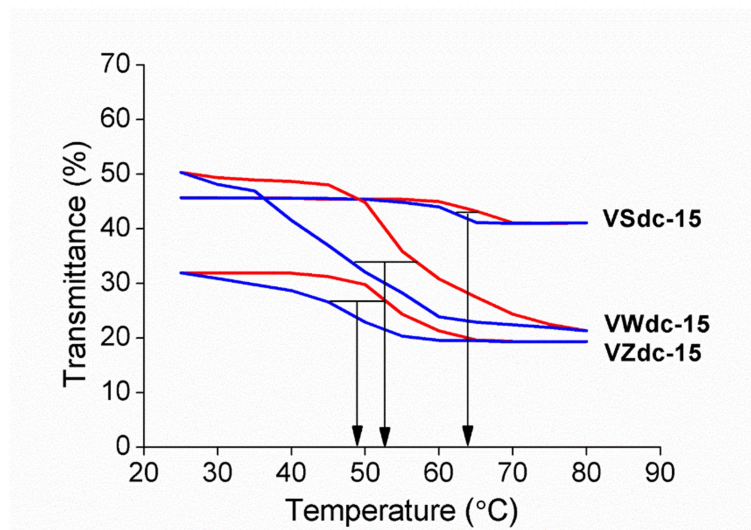


Fig. 6. Representative NIR transmittance hysteresis plots recorded at 1300 nm for selected bilayer films of VO_2 with ZnO , SnO_2 and WO_3 top-layers. Heating and cooling are indicated by red and blue lines, respectively. The values of T_c are taken as the mid points of the width of the hysteresis, as shown.

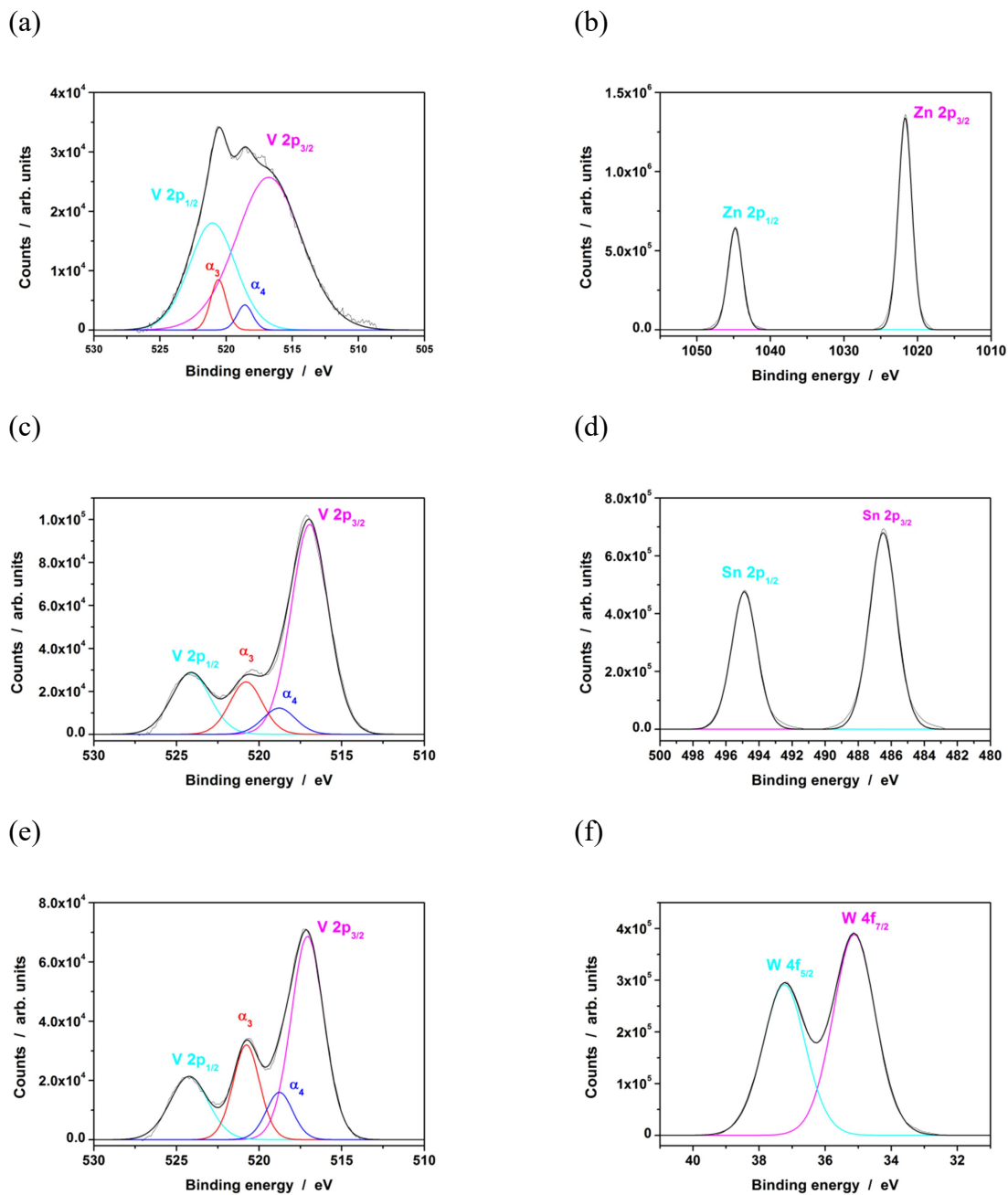


Fig. 7. Fitted XPS spectra for representative bilayer films: (a) VZdc-15 V spectrum, (b) VZdc-15 Zn spectrum, (c) VSdc-15 V spectrum (d) VSdc-15 Sn spectrum, (e) VWdc-15 V spectrum and (f) VWdc-15 W spectrum.

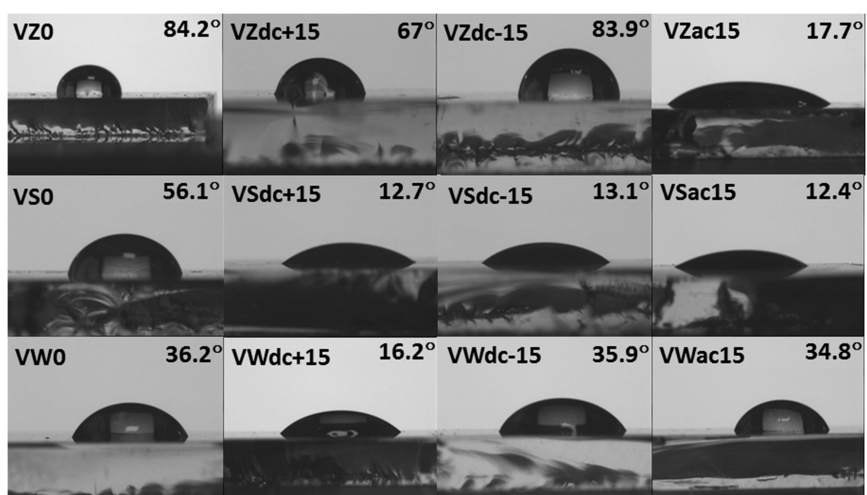


Fig. 8. Water contact angle images taken for bilayer films of VO_2/ZnO , VO_2/SnO_2 and VO_2/WO_3 .

Supporting Information

Improved thermochromic properties in bilayer films of VO₂ with ZnO, SnO₂ and WO₃ coatings for energy efficient glazing.

I. Top, R. Binions, C. Sol, I. Papakonstantinou, M. Holdynski, S. Gaiaschi and I. Abrahams

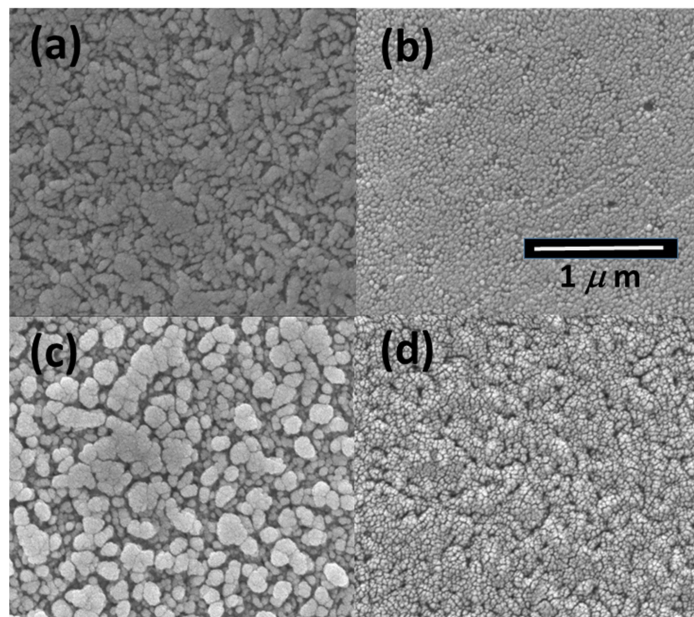


Fig. S1. SEM images of VO₂ single-layer films produced under different electric fields (a) zero field, (b) +15 V DC, (c) -15 V DC and (d) 15 V AC. All images were taken at 100000 × magnification.

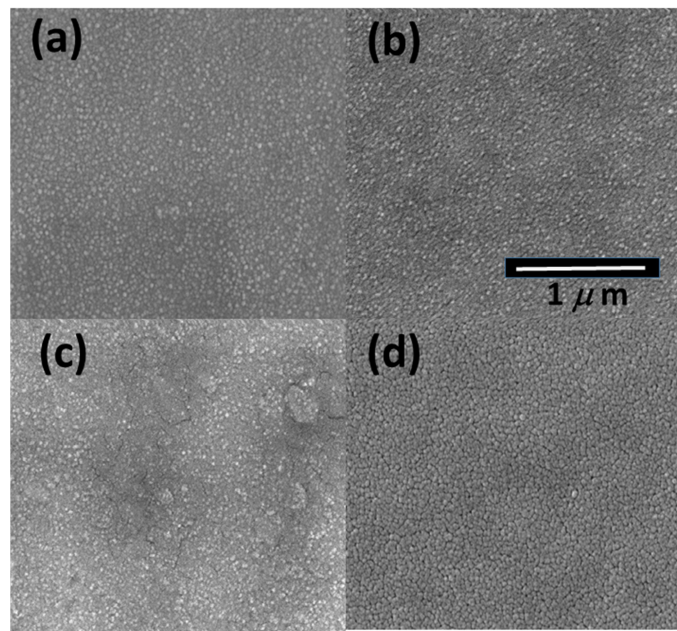


Fig. S2. SEM images of VO₂/ZnO bilayer films (a) VZ0, (b) VZdc+15, (c) VZdc-15 and (d) VZac15. All images were taken at 100000 × magnification.

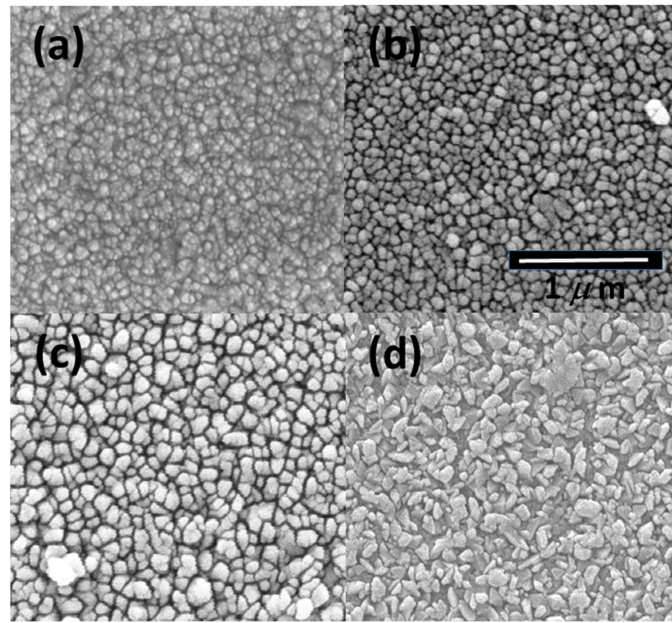


Fig. S3. SEM images of VO_2/SnO_2 bilayer films: (a) VS0, (b) VSdc+15, (c) VSdc-15 and (d) VSac15. All images were taken at $100000\times$ magnification.

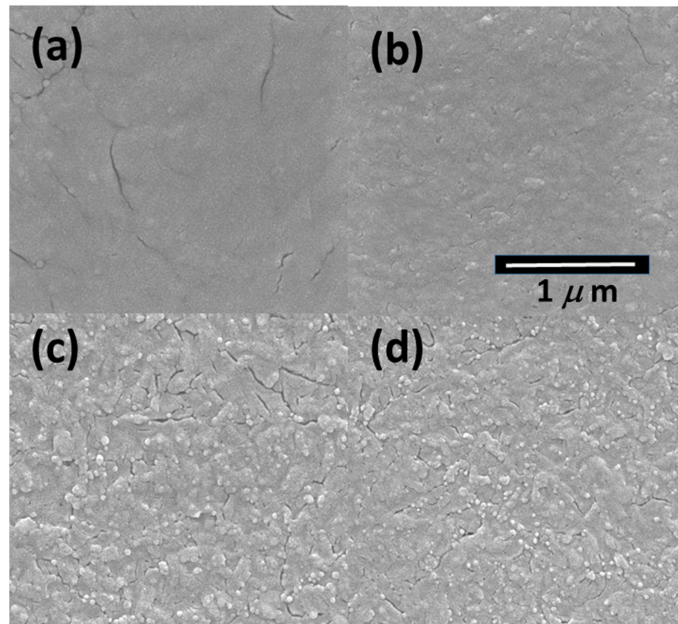


Fig. S4. SEM images of VO_2/WO_3 bilayer films: (a) VW0, (b) VWdc+15, (c) Wdc-15 and (d) VWac15. All images were taken at $100000\times$ magnification.

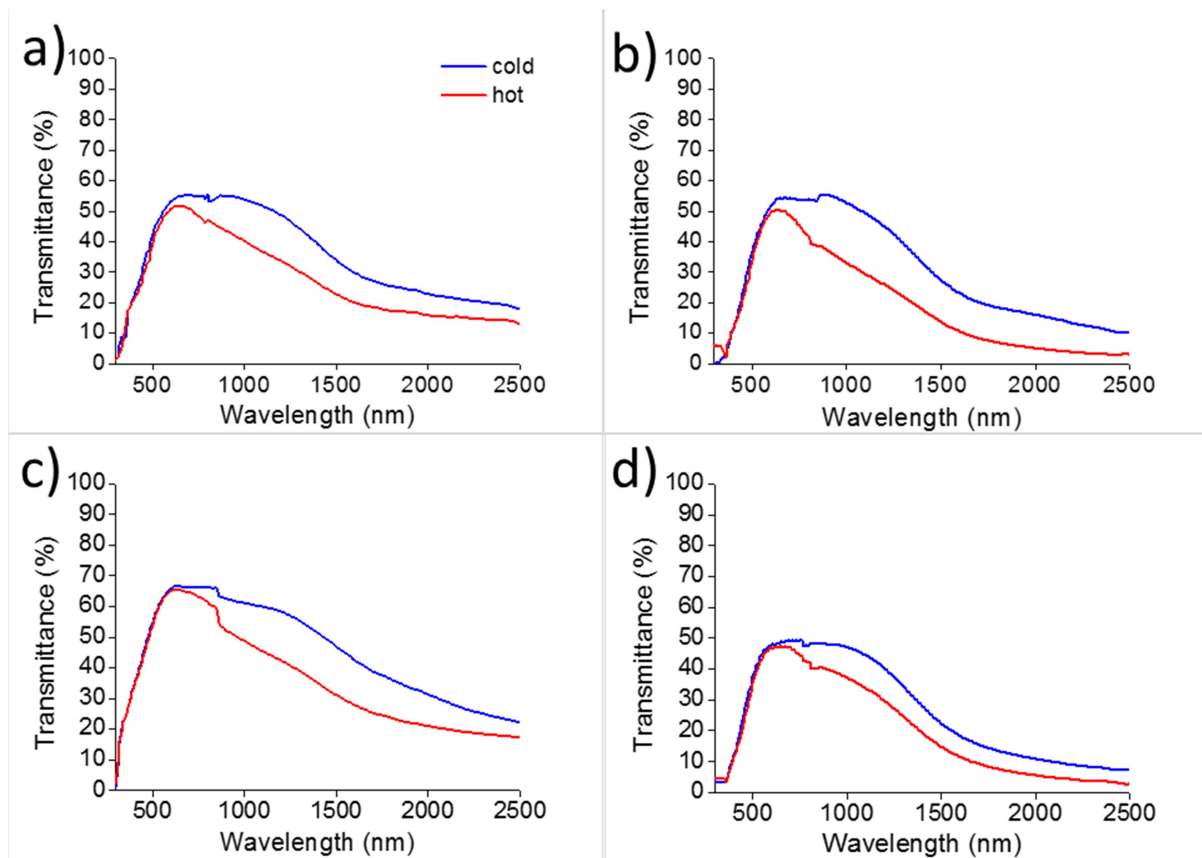


Fig. S5. Hot and cold UV-Vis-NIR transmittance spectra for ZnO coated bilayer films: (a) VZ0, (b) VZdc+15 and (c) VZdc-15, (d) VZac15 where red and blue lines represent hot and cold stages, respectively.

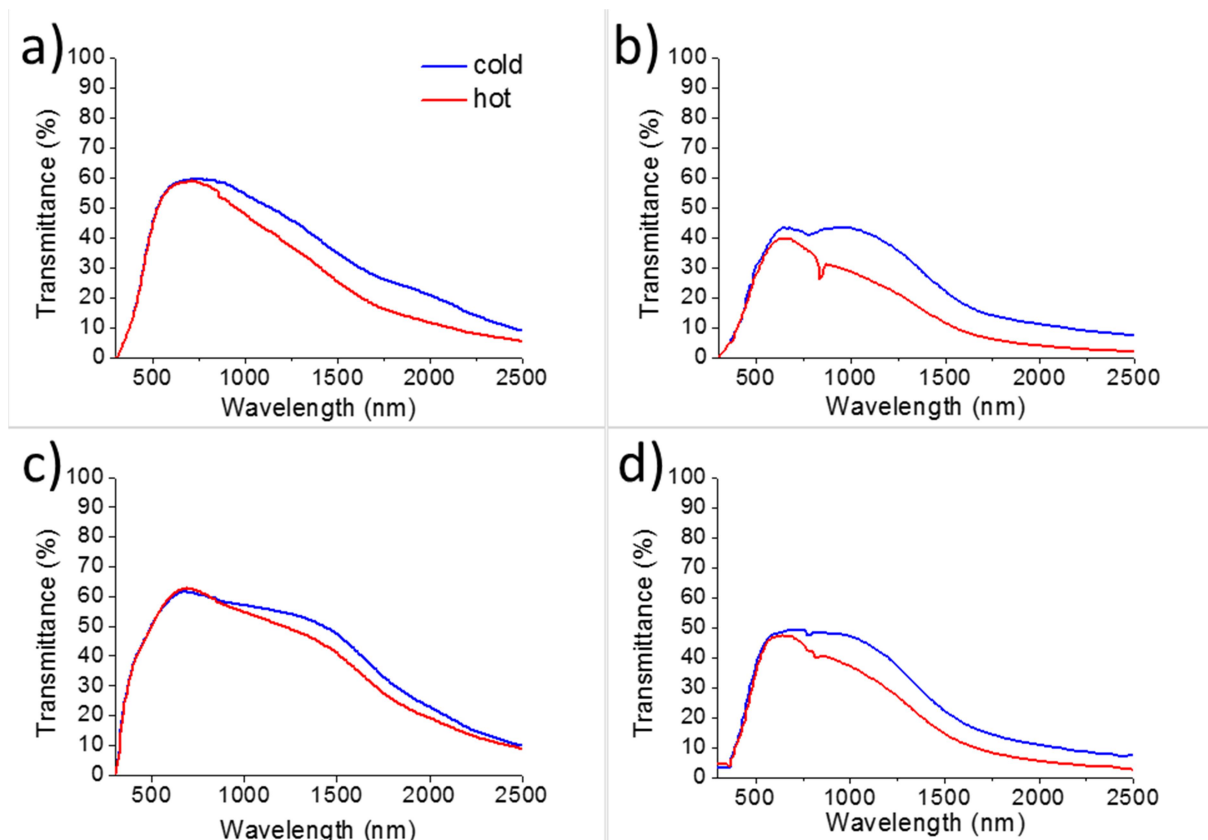


Fig. S6. Hot and cold UV-Vis-NIR transmittance spectra for SnO₂ coated bilayer films: (a) VS0, (b) VSdc+15 and (c) VSdc-15, (d) VSac15 where red and blue lines represent hot and cold stages, respectively.

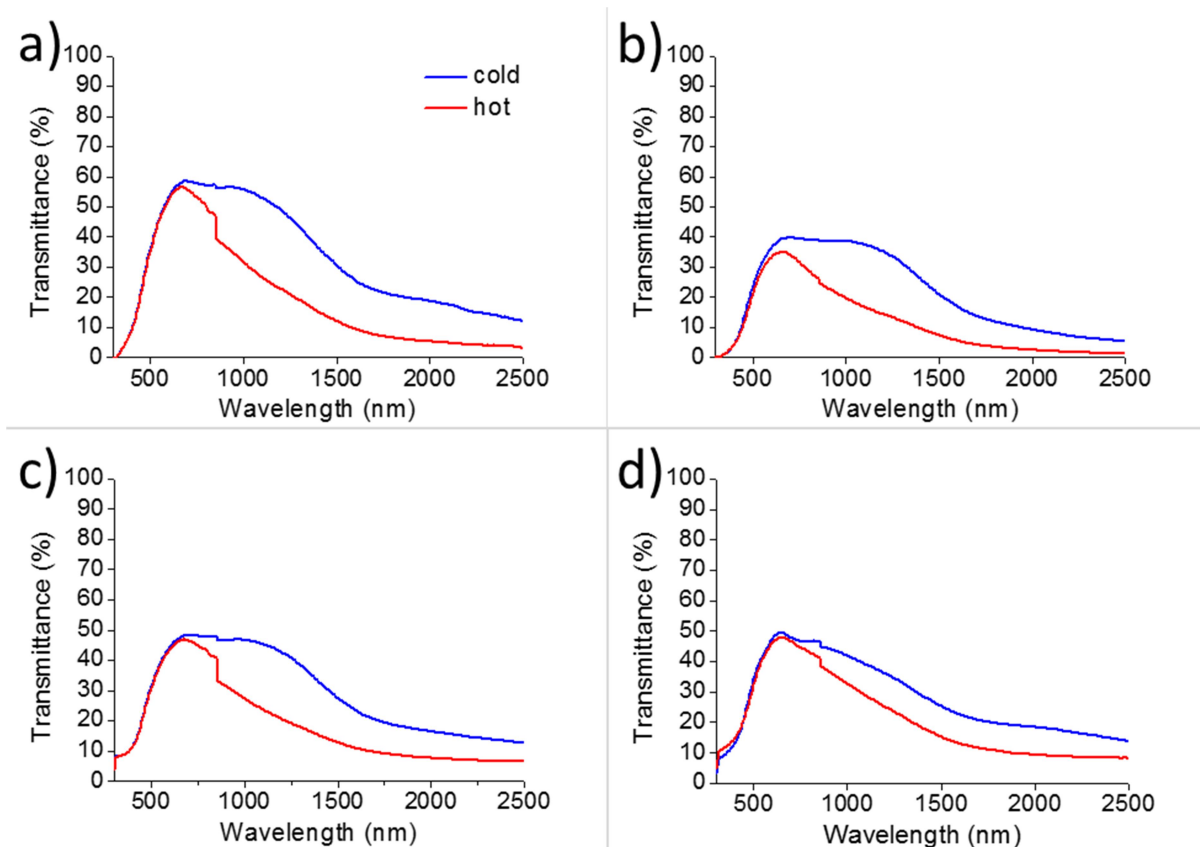


Fig. S7. Hot and cold UV-Vis-NIR transmittance spectra for WO₃ coated bilayer films: (a) VW0, (b) VWdc+15 and (c) VWdc-15, (d) VWac15 where red and blue lines represent hot and cold stages, respectively.

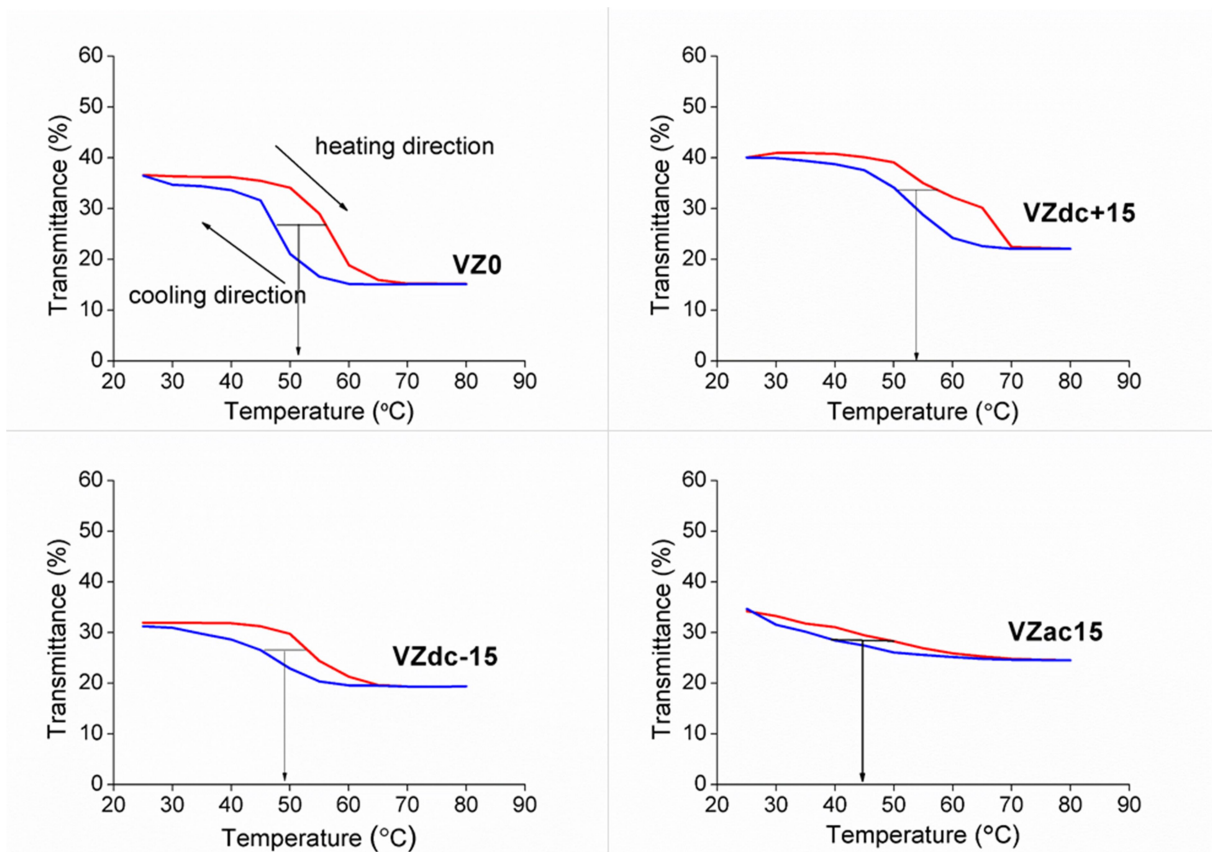


Fig. S8. NIR transmittance hysteresis plots recorded at 1300 nm for ZnO coated bilayer films: (a) VZ0, (b) VZdc+15 and (c) VZdc-15, (d) VZac15. Heating and cooling are indicated by red and blue lines, respectively. The values of T_c are taken as the mid points of the width of the hysteresis, as shown.

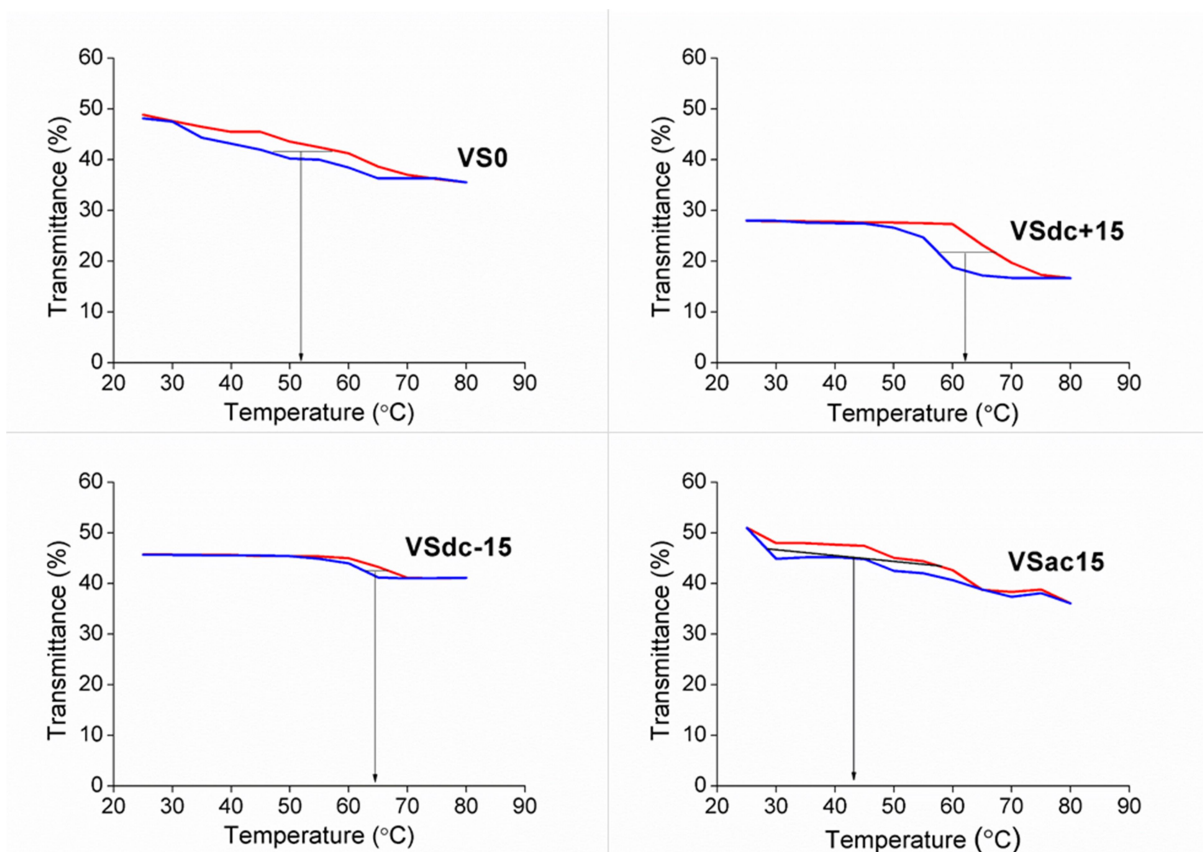


Fig. S9. NIR transmittance hysteresis plots recorded at 1300 nm for SnO₂ coated bilayer films: (a) VS0, (b) VSdc+15 and (c) VSdc-15, (d) VSac15. Heating and cooling are indicated by red and blue lines, respectively. The values of T_c are taken as the mid points of the width of the hysteresis, as shown.

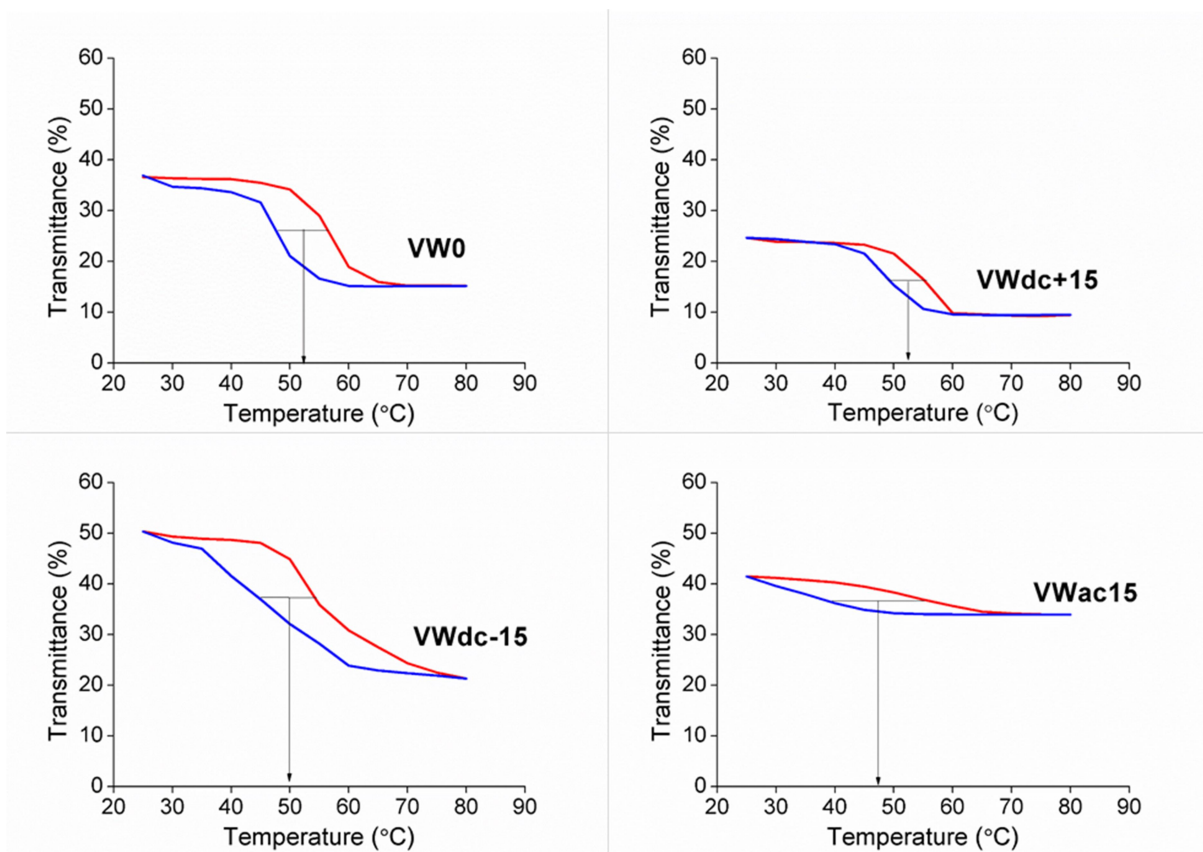


Fig. S10. NIR transmittance hysteresis plots recorded at 1300 nm for WO₃ coated bilayer films: (a) VW0, (b) VWdc+15 and (c) VWdc-15, (d) VWac15. Heating and cooling are indicated by red and blue lines, respectively. The values of T_c are taken as the mid points of the width of the hysteresis, as shown.

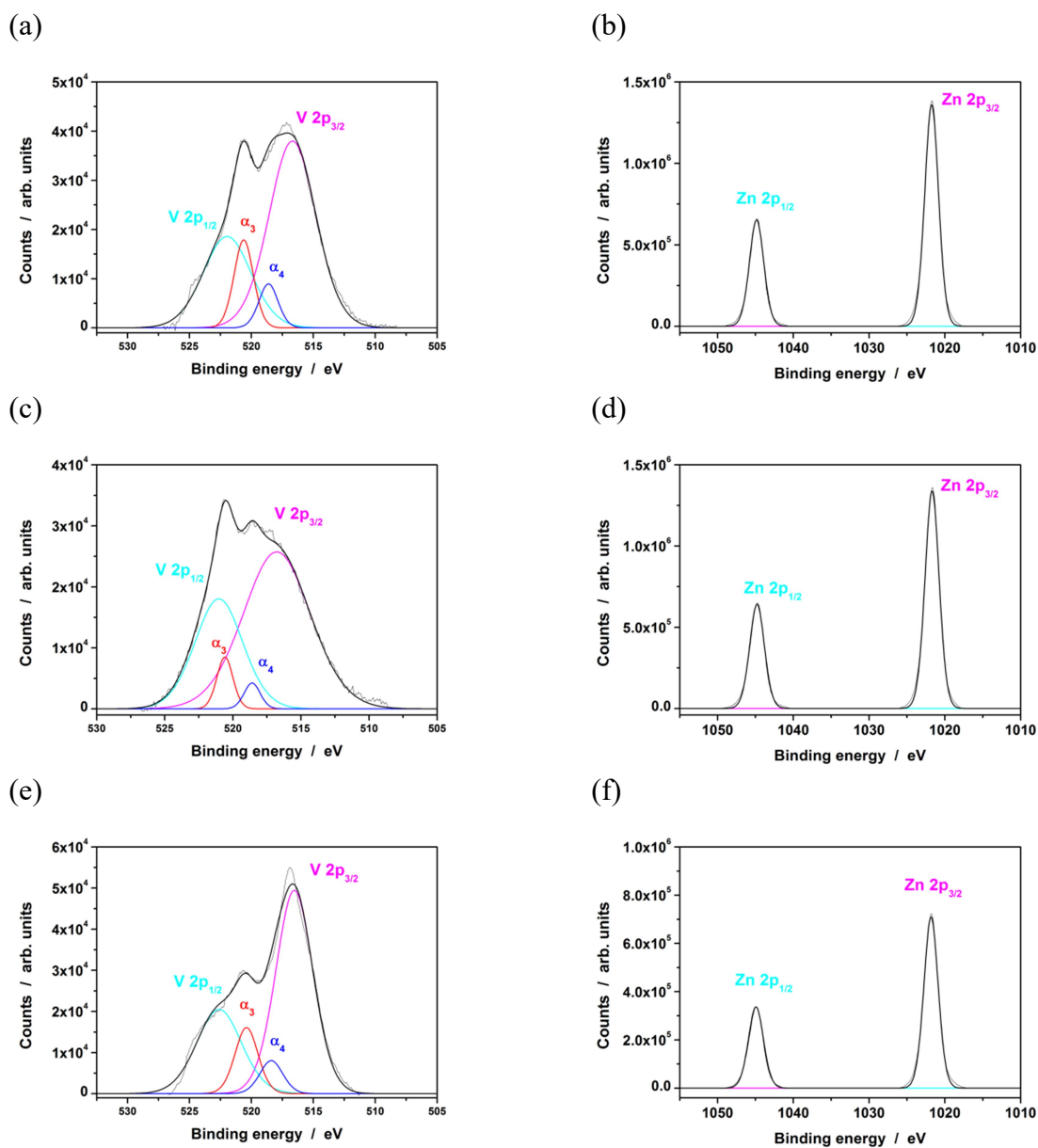


Figure S11. Fitted XPS spectra for ZnO coated bilayer films: (a) VZ0 V spectrum, (b) VZ0 Zn spectrum, (c) VZdc-15 V spectrum (d) VZdc-15 Zn spectrum, (e) VZdc+15 V spectrum and (f) VZdc+15 Zn spectrum.

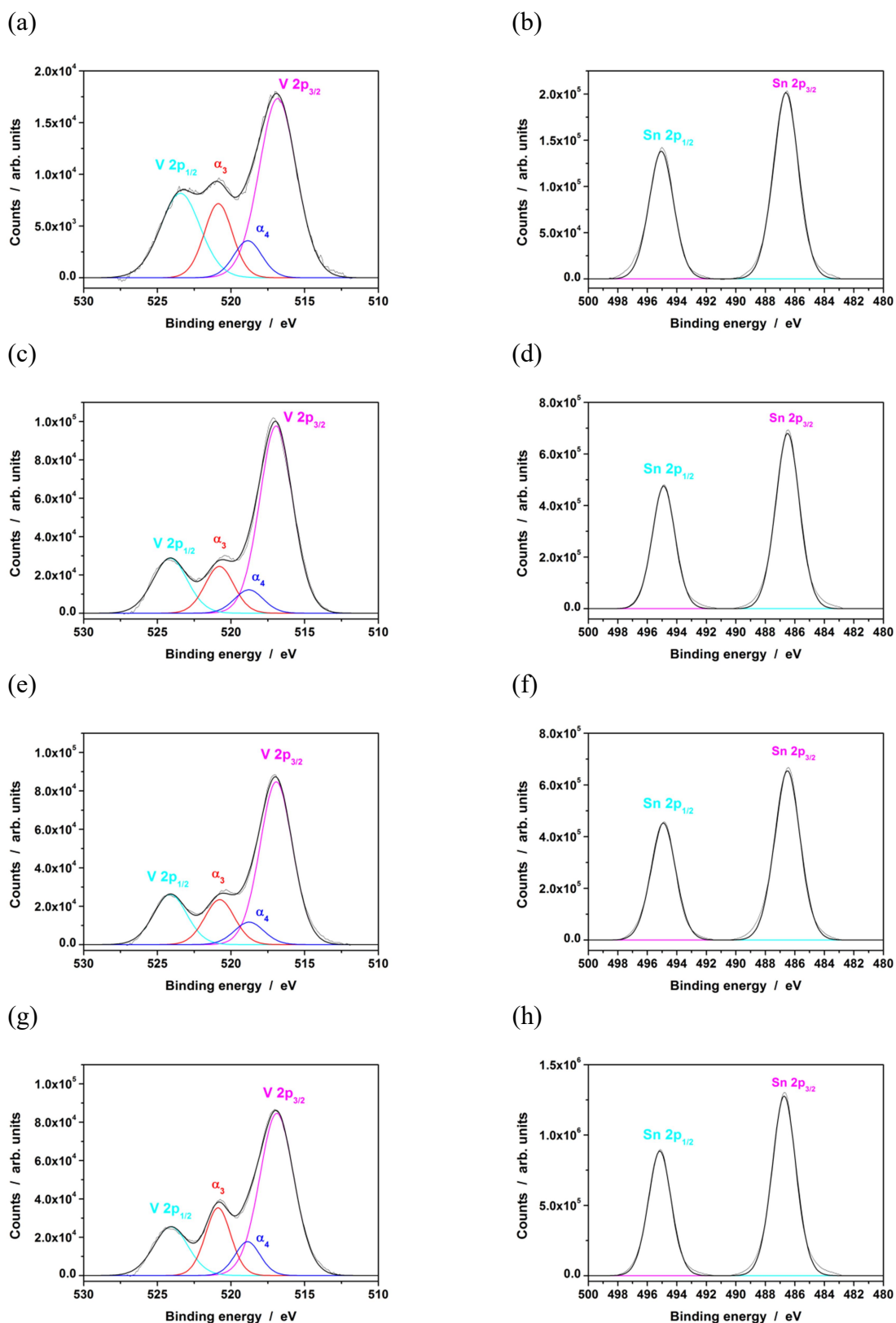


Figure S12. Fitted XPS spectra for SnO₂ coated bilayer films: (a) VS0 V spectrum, (b) VS0 Sn spectrum, (c) VSdc-15 V spectrum (d) VSdc-15 Sn spectrum, (e) VSdc+15 V spectrum, (f) VSdc+15 Sn spectrum, (g) VSac15 V spectrum and (h) VSac15 Sn spectrum.

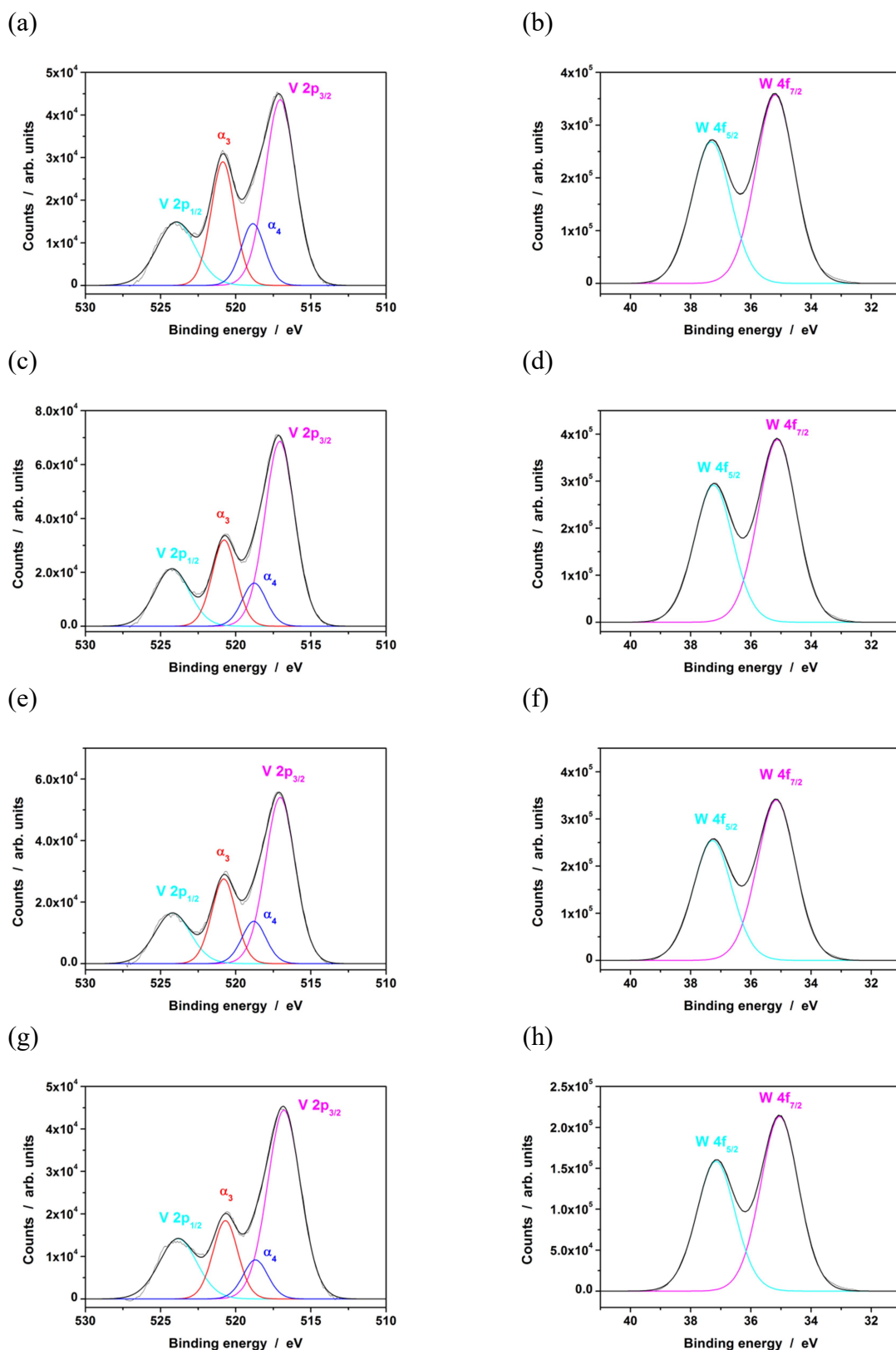


Figure S13. Fitted XPS spectra for WO_3 coated bilayer films: (a) VW0 V spectrum, (b) VW0 W spectrum, (c) VWdc-15 V spectrum (d) VWdc-15 W spectrum, (e) VWdc+15 V spectrum, (f) VWdc+15 W spectrum, (g) VWac15 V spectrum and (h) VWac15 W spectrum.